Energy Storage Materials 52 (2022) 94–103

Contents lists available at ScienceDirect

Energy Storage Materials

journal homepage: www.elsevier.com/locate/ensm

Realizing rapid electrochemical kinetics of Mg^{2+} in Ti-Nb oxides through a Li^+ intercalation activated strategy toward extremely fast charge/discharge dual-ion batteries

Dongzheng Wu, Fei Wang, Huiya Yang, Yaoqi Xu, Yichao Zhuang, Jing Zeng *, Yang Yang *, Jinbao Zhao *

State Key Lab of Physical Chemistry of Solid Surfaces, Collaborative Innovation Centre of Chemistry for Energy Materials, State-Province Joint Engineering Laboratory of Power Source Technology for New Energy Vehicle, Engineering Research Center of Electrochemical Technology, Ministry of Education, College of Chemistry and Chemical Engineering, Xiamen University, Xiamen 361005, PR China

ARTICLE INFO

Keywords:
$TiNb_2O_7$
Electron self-acceleration
Mg^{2+}/Li^+ co-intercalation
High-rate materials
In situ Raman spectroscopy
Dual-ion batteries

ABSTRACT

The development of practical magnesium batteries is severely hindered by the sluggish solid diffusion processes resulting from the relatively high charge density of Mg^{2+} with two unit charges. Therefore, exploiting novel charge storage mechanisms to overcome the inherent kinetic obstruction is urgently needed. Herein, the rapid diffusion kinetics of Mg^{2+} in Wadsley-Roth phase $TiNb_2O_7$ (TNO) is realized through the electrochemical Li^+ intercalation boosted approach, contributing to the successful fabrication of high-rate and ultra-long lifespan dual-ion batteries. Through adding lithium salt into the conventional all phenyl complex electrolyte, not only Li^+ but also Mg^{2+} can be intercalated into the TNO, implying the intercalation of Mg^{2+} can be activated by the intercalation of Li^+. Meanwhile, theoretical calculations reveal that the insertion of Li^+ can significantly improve the electronic conductivity of TNO and reduce the diffusion energy barrier of Mg^{2+} in TNO. Moreover, in-situ Raman and ex-situ X-ray diffraction measurements also indicate the improved structural integrity of TNO with Li^+ pre-intercalation during cycling. Consequently, such a dual-ion battery system with the TNO cathode and Mg metal anode exhibits a high reversible capacity (243.6 mAh g^{-1} at 0.1 C) and excellent high-rate cycling stability (capacity retention of 85.1% at 5 C after 2000 cycles)

1. Introduction

Lithium-ion batteries (LIBs) have been widely used in portable devices due to their high energy density, which also bring a lot of convenience to mankind and promote the progress of society [1–4]. However, with the newly emerging application scene of large-scale electrochemical energy storage, the potential safety hazards and price issues of LIBs have attracted increasing attention. Therefore, the development of an alternative battery system with the features of low cost and high safety is highly desired [5–9]. Rechargeable magnesium batteries (RMBs) are one of the most promising technologies for large-scale applications due to their high safety and rich crustal content of Mg. Moreover, the high volumetric energy density (3833 mAh cm^{-3}) and the low electrode potential (-2.37 V vs. S.H.E.) of RMBs have also become the focuses of attention [10–18].

Despite these potential superiorities, the development of practical RMBs still faces serious challenges, mainly resulting from the immature cathode materials and electrolytes [19–27]. In terms of cathode materials, the sluggish solid-state diffusion kinetics of Mg^{2+} fails to achieve reversible and fast intercalation/deintercalation of Mg^{2+} in most materials. Targeting at the inherent defects restricting the diffusion kinetics, diverse modification strategies have been proposed. Constructing nanoparticles is an effective way to shorten the diffusion path of Mg^{2+} and provides more active sites for Mg^{2+} [28]. However, through this method, those materials that cannot achieve the Mg^{2+} intercalation/deintercalation still cannot serve as cathode materials for Mg storage. Subsequently, the construction of interlayer engineering of layered compounds has also been proposed. Pre-intercalated cationic, H_2O, or polymer is a feasible approach to widen layer spacing of layered cathode materials, endowing the Mg storage capability for many two-dimensional materials [29–31]. Although many efforts have been devoted, these improvements in electrochemical reversibility are mainly

* Corresponding authors.
E-mail addresses: zengjing@xmu.edu.cn (J. Zeng), yangyang419@xmu.edu.cn (Y. Yang), jbzhao@xmu.edu.cn (J. Zhao).

https://doi.org/10.1016/j.ensm.2022.07.042
Received 5 May 2022; Received in revised form 23 July 2022; Accepted 28 July 2022
Available online 29 July 2022

achieved based on a relatively low cycling current density (< 0.5 C), which are still hardly to meet the requirements of practical applications [32–35].

In recent years, Wadsley-Roth phase $TiNb_2O_7$ (TNO) with excellent rate performance and high theoretical capacity (387.6 mAh g^{-1}) has been extensively studied as high-rate electrode materials for Li^+ storage [36–38]. Li^+ tends to be reversibly intercalated into the 110 plane of TNO, exhibiting outstanding structural stability and good rate performance in LIBs [39,40]. It is interesting that, with the increase of the Li^+ intercalation, the electronic conductivity of TNO will be enhanced simultaneously [37]. The outstanding advantages of TNO in both Li^+ and electron transport imply that its lattice host may be also appropriate for facile Mg^{2+} (de)intercalation processes. However, the reversible Mg^{2+} storage of TNO is rarely reported in previous studies, which may be due to the sluggish diffusion kinetics of high charge density of Mg^{2+} with two unit charges.

Herein, the highly reversible and rapid Mg^{2+} storage performance in TNO is successfully activated thorough a Li^+ electrochemical pre-intercalation strategy. By adding lithium salt into the conventional all phenyl complex (APC) electrolyte, the preceding intercalation of Li^+ in TNO can weaken the electrostatic interaction between the crystal structure of TNO and Mg^{2+}, leading to the enhanced Mg^{2+} intercalation kinetics. Meanwhile, the pre-intercalated Li^+ can also alleviate the volume change caused by the intercalation of Mg^{2+} into TNO, achieving the excellent structural stability during ions (de)intercalation processes. Although TNO is a typical semiconductor, the Li^+ pre-intercalated phase of $Li_xTiNb_2O_7$ is surprising transformed to a metallic conductor, achieving electron self-acceleration during discharging process and further promoting subsequent intercalation of ions. Consequently, the synergetic enhancement of electron transport, ion diffusion and structural integrity of TNO during Li^+/Mg^{2+} co-intercalation process makes it a promising host structure for fabricating high-rate dual-ion batteries.

2. Experimental section

2.1. Material preparation

Graphene is introduced to further improve the electronic conductivity of TNO (TNO/G) and the synthesis method was reported by our previous work [37]. For a typical synthesis of TNO, 0.17 g of tetrabutyl titanate was added to an appropriate amount of dilute ammonia and stirred for 10 min. Subsequently, 1.5 mL of 12 M concentrated nitric acid was added. When the mixture dissolved and the solution became a clear liquid, 1.5 g of glycine and 0.65 g of hydrated niobium oxalate were added under continuous stirring for 3 h. Then the mixture was calcined in air at 900 °C for 1 h. For the typical synthesis of TNO/G, 0.3 g TNO and 3 mL Poly(diallyl dimethyl ammonium chloride) were added in 50 mL water under ultrasonic treatment. Then the mixed solution was centrifuged to collect TNO and the TNO was added in 25 mL water. Then this solution was added drop by drop to 30 mL of graphene oxide aqueous dispersion (1 mg/mL). After that, the mixed solution was frozen with sufficient liquid nitrogen and freeze-dried for 24 h. Finally, TNO/G was obtained by calcining the mixture at 700 °C under an Ar atmosphere for 3 h.

2.2. Materials characteristic

The crystal structures of samples were characterized by X-ray diffraction (XRD) on Rigaku Ultima IV. The morphologies of samples were recorded by scanning electron microscopy (SEM, Zeiss GeminiSEM 500) and high-resolution transmission electron microscopy (HRTEM, Tecnai F30), respectively. The Raman spectra were ascertained by Raman spectroscope (Horiba Xplora). The valence state of samples was analyzed by X-ray photoelectron spectroscopy (XPS, PHI Quantum 2000).

2.3. Electrochemical measurements

The APC electrolyte was prepared according to previous reports [41]. Typically, 0.5 M $AlCl_3$ solution was prepared by adding 0.53 g $AlCl_3$ into 8 mL tetrahydrofuran (THF) slowly. 8 mL THF was added to 4 mL 2.0 M PhMgCl to get 0.67 M PhMgCl solution. The two solutions were mixed and stirred for 24 h to obtain APC electrolyte (0.4 M 2PhMgCl-$AlCl_3$/THF). To prepared hybrid electrolyte, appropriate amount of LiCl was added to the APC and stirred overnight. All the preparations were operated in glove box filled under Ar atmosphere. The slurry composed of 70 wt% TNO/G, 20 wt% acetylene black, 10 wt% polyvinylidene fluoride (PVDF) was casted on Ti foil and dried at 80 °C. The mass loading was about 1.5 mg of active material. Electrochemical performances were tested by using 2032 coin-type cell with fresh polished Mg as the counter electrode. The electrochemical tests were conducted in the potential range of 0.2 ~ 2.0 V vs. Mg^{2+}/Mg. The CV tests at various scan rates were taken after 10 activation cycles at 0.1 C. All the electrochemical measurements were performed at room temperature.

2.4. Calculation methodology

All the density functional theory (DFT) calculations were operated by using Vienna Ab Initio Simulation Package (VASP) [42]. The projector augmented wave potentials were used to calculate the electronic exchange-correlation interaction along with the Generalized Gradient Approximation functional in the parameterization of the Perdew Burke and Ernzerhof pseudopotential [43,44]. The cut off energy for the wave function was set to 450 eV. Geometry optimizations were operated until all the forces were less than 0.02 eV/Å per atom. A k-point mesh with a spacing of ca. 0.03 A^{-1} was adopted. The long-range interactions (DFT-DF3) are considered as a correction in all calculations. In addition, for the Ti and Nb atoms, the U schemes need to be applied, and the U has been set as 5.0 and 4.0 eV. The climbing image nudged elastic band (CI-NEB) method was adopted to calculate diffusion barriers of Mg^{2+} in TNO, and $LiTiNb_2O_7$ (LiTNO) [45,46]. The intercalation formation energies of atom in TNO and LiTNO were calculated according to Eq. (1) as follows:

$$E_{form} = E(\text{intercalated}) - E(\text{pristine}) - E(\text{M}) \quad (1)$$

where E(intercalated) and E(pristine) are the total energies of atom intercalated and pristine TNO (or LiTNO). E(M) is the energy per atom of the metal. And the voltage of Mg^{2+} or Li^+ insertion was calculated according to Eq. (2) as follows:

$$V = -\frac{E_{form}}{N} \quad (2)$$

Where N is the number of electrons transferred.

3. Results and discussions

As shown in Fig. 1a, the crystal structure of TNO exhibits large enough channels for the diffusion of Mg^{2+} with an ionic radius of 0.72 Å and enough empty sites for the intercalation of Mg^{2+}, implying that TNO is a potential material for Mg storage. However, as shown in Fig. S1, the discharge-charge profiles of TNO/G with pure APC electrolyte at 0.1 C present negligible discharge capacity, indicating the intercalation/deintercalation of Mg^{2+} cannot be achieved inside TNO/G. And the inhibition of Mg storage properties in TNO/G may be caused by the large electrostatic interaction between Mg^{2+} and the lattice host of TNO crystal structure and the poor inherent electronic conductivity of TNO. Herein, the electrochemical Li^+ pre-intercalation strategy is expected to break the shackles and releases the potential Mg storage capability of TNO. The feasibility of this promising approach was investigated through DFT calculations firstly. Unexpectedly, after Li^+ inserts into the crystal structure of TNO, the intercalation of Mg^{2+} can be activated. And

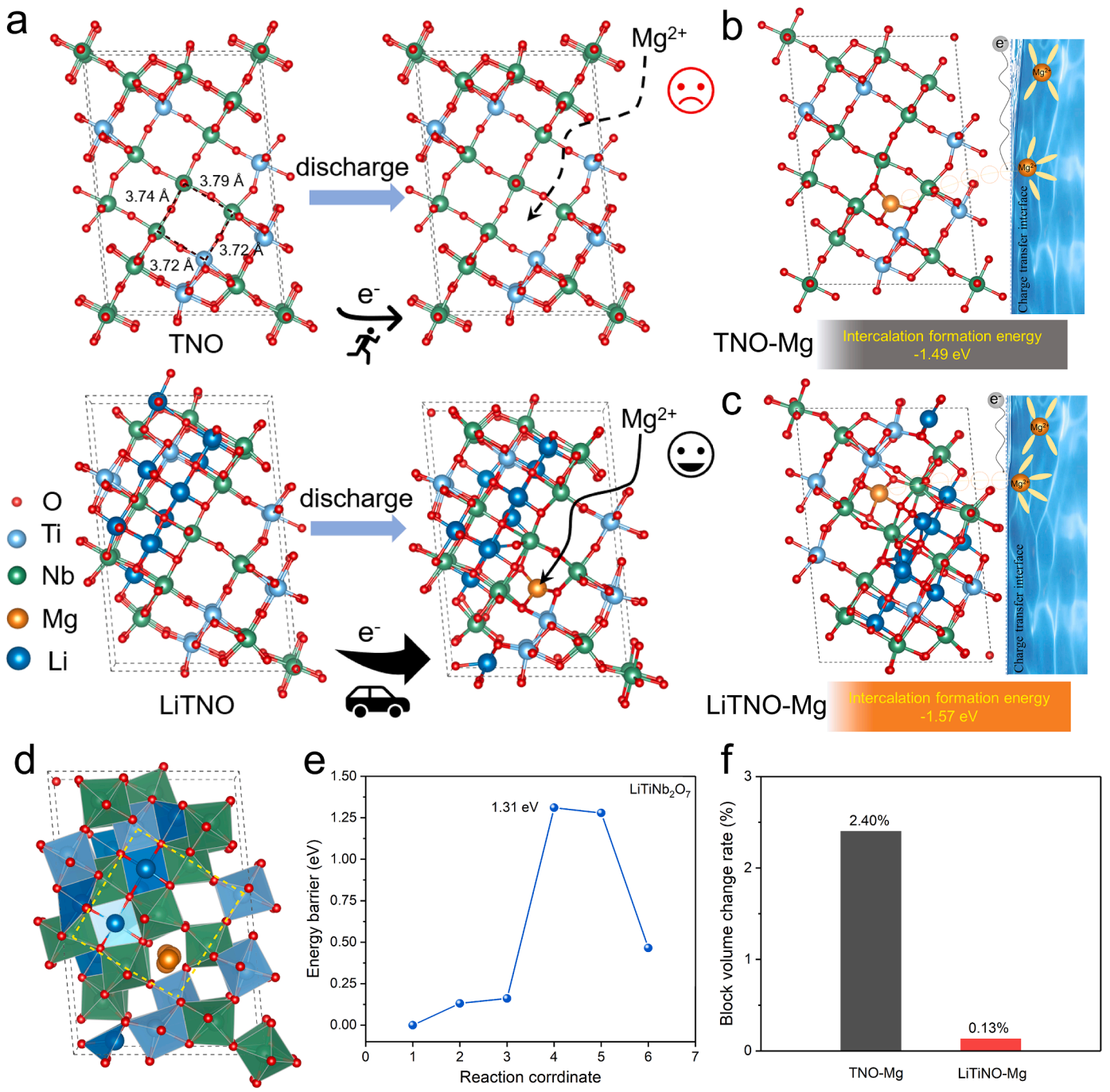

Fig. 1. (a) Schematic illustration of the charge storage mechanism of TNO and LiTNO. Intercalation formation energies when Mg^{2+} is intercalated into (b) TNO and (c) LiTNO. (d) Diffusion path of Mg^{2+} inside the $LiTiNb_2O_7$ crystal structure and the block of $LiTiNb_2O_7$ crystal structure marked by yellow dotted line. (e) Mg^{2+} diffusion energy barriers of $LiTiNb_2O_7$. (f) Block volume change rate of TNO and LiTNO after Mg intercalation through theoretical calculations.

the preceding intercalation of Li^+ can effectively improve the electronic conductivity of TNO cathode material, achieving electron self-acceleration during discharging process and benefitting to subsequent intercalation of ions [37]. The unique properties of the TNO and $LiTiNb_2O_7$ (LiTNO) materials were also verified by theoretical calculations. As shown in Fig. S2, after calculation, the band gap of TNO is 2.15 eV, indicating that TNO is a semiconductor. LiTNO presents a higher density of state (DOS) than TNO at the Fermi level, implying that the TNO has been a conductor after Li^+ intercalation. After more Li^+ ions are intercalated, the $Li_2TiNb_2O_7$ and $Li_{3.5}TiNb_2O_7$ are still good conductors with better electronic conductivity than TNO. These results indicate that the electron self-acceleration process exists inside TNO during the earlier ion intercalation process. Besides, simulation calculations of thermodynamics were also conducted to simulate the intercalation of ions in TNO and LiTNO. Firstly, the intercalation voltages of Li^+ and Mg^{2+} in TNO were calculated and the results are shown in Fig. S3a. The results demonstrate that When Li^+ is intercalated into TNO, the Li^+ tends to occupy the interstitial site there and the corresponding intercalation voltage is 1.21 V. When Mg^{2+} is intercalated into TNO, the Mg^{2+} tends to occupy the same sites and the corresponding intercalation voltage is 0.74 V. The above calculation results indicate that the Li^+ is preferred to be inserted into TNO thermodynamically. Besides, in order to verify the consistency of the DFT models and the experimental results, the results of experimental and calculated were collected for

comparison. As shown in Fig. S3b, c, the experimental XRD patterns of pristine TNO electrode and TNO electrode discharged to 0.7 V are consistent with that of calculated XRD patterns of TNO and LiTNO-Mg, indicating that the DFT models are reliable. Subsequently, based on the rational DFT models, the intercalation formation energies of Mg^{2+} in TNO and LiTNO were calculated. As shown in Fig. 1b,c, Mg^{2+} tends to insert into the crystal structure of LiTNO with the more favorable intercalation formation energy (-1.57 eV) than TNO (-1.49 eV). Besides, Mg^{2+} can be inserted into the crystal structure of LiTNO easier due to the higher electronic conductivity of LiTNO which further shortens the electron transport path. Furthermore, based on the rational construction of Mg^{2+} diffusion path inside the TNO and LiTNO crystal structure, the behavior of Mg^{2+} diffusion is studied (Figs. 1d, e and S4) [47]. The Mg^{2+} diffusion energy barrier of LiTNO (1.31 eV) is smaller than that of TNO (1.33 eV), indicating that the transport kinetics of Mg^{2+} is rapid in tunnel of LiTNO. Benefitting from the preceding intercalation of Li^{+}, it can effectively weaken the electrostatic interaction between the O atoms and Mg^{2+} and reduce the Mg^{2+} diffusion energy barrier. Consequently, Mg^{2+} can be inserted into the LiTNO due to the intercalation of Li^{+}. Moreover, as shown in Fig. 1f, after Mg^{2+} inserts into the LiTNO, the block volume change rate of LiTNO-Mg (0.13%) is smaller than that of TNO-Mg (2.4%) through the theoretical calculations. Combining with the results of thermodynamic simulations and diffusion dynamics, the introduction of Li^{+} into TNO facilitates the intercalation reaction and diffusion kinetics of Mg^{2+} and alleviates the volume change during the Mg intercalation process, indicating the superiority of Li^{+} pre-intercalation approach by theoretical calculations.

As shown in Fig. 2a, the XRD patterns of TNO and TNO/G can be well indexed to the $TiNb_2O_7$ (JCPDS No.77-1374) without crystal impurities. As shown in Fig. 2b, Raman spectrum of TNO can be well matched with previous reports [37,39]. After the introduction of graphene, the Raman spectrum of TNO/G composite material shows obvious signals of graphene (around 1352 and 1598 cm^{-1}), corresponding to the D-band and G-band, respectively. And the remaining peaks correspond to the signal peaks of TNO. This structure can improve the electronic conductivity of the TNO/G composite electrode. XPS spectra of TNO/G were also performed to confirm the valence state of element in TNO/G (Figs. 2c, d and S5). In Fig. 2d, the C 1s spectrum can be split to three peaks located at 284.8 eV (C-C), 285.7 eV (C-O) and 288.8 eV (C=O), which proves the introduction of graphene. The XPS spectrum of Nb 3d two peaks is exhibited in Fig. S5a and presents at about 207.9 and 210.8 eV, corresponding to Nb^{5+} in TNO/G. Besides, as shown in Fig. S5b, XPS spectrum of Ti 2p indicates that Ti 2p 1/2 and Ti 2p 3/2 peaks are located at about 465.2 eV and 459.5 eV, corresponding to Ti^{4+} in TNO/G.

SEM and TEM images were taken to further verify the morphology of TNO/G. As shown in Fig. 2e, the structure of graphene wrapped TNO can be observed. In addition, it can be more clearly observed from the TEM images (Fig. 2f, g) that the size of TNO nanoparticles is about 50–150 nm and the TNO nanoparticles are well encapsulated in graphene sheets. As shown in Fig. 2h, the HRTEM of TNO/G exhibits good crystallinity of TNO. The interplanar distance of crystal is measured to be 0.27 nm, corresponding to the 203 plane of TNO. And amorphous graphene can be observed at the edge of the TNO particle, indicating the good electronic connectivity between TNO and graphene. The element mapping of Ti, Nb, O, and C elements in TNO/G is shown in Fig. 2i, proving the uniform distribution of all elements. The above data shows the successful synthesis of TNO/G material.

In order to explore the optimal amount addition of Li^{+}, various amounts of LiCl were added into APC to investigate the electrochemical performance of TNO/G. The voltage profiles of TNO/G in APC with various amounts of LiCl at 0.1 C is shown in Fig. 3a. TNO/G shows a negligible discharge capacity in pure APC electrolyte due to the sluggish

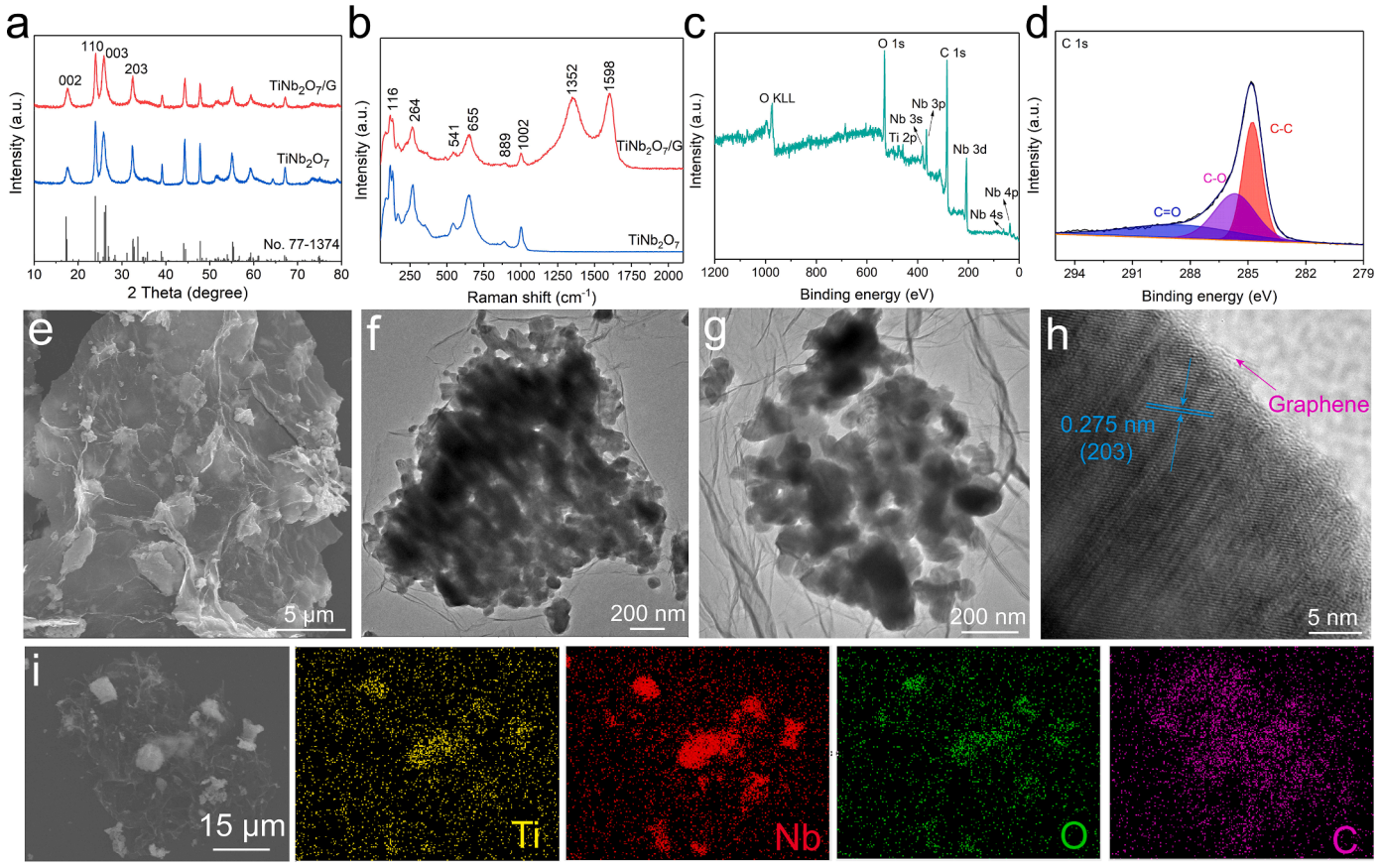

Fig. 2. (a) XRD patterns and (b) Raman spectra of TNO and TNO/G. (c) The XPS spectrum of the TNO/G powder. (d) The XPS spectra of C 1s of the TNO/G. (e) SEM image of TNO/G. (f, g) TEM images and (h) HRTEM image of TNO/G. (i) Elemental mapping of TNO/G powder.

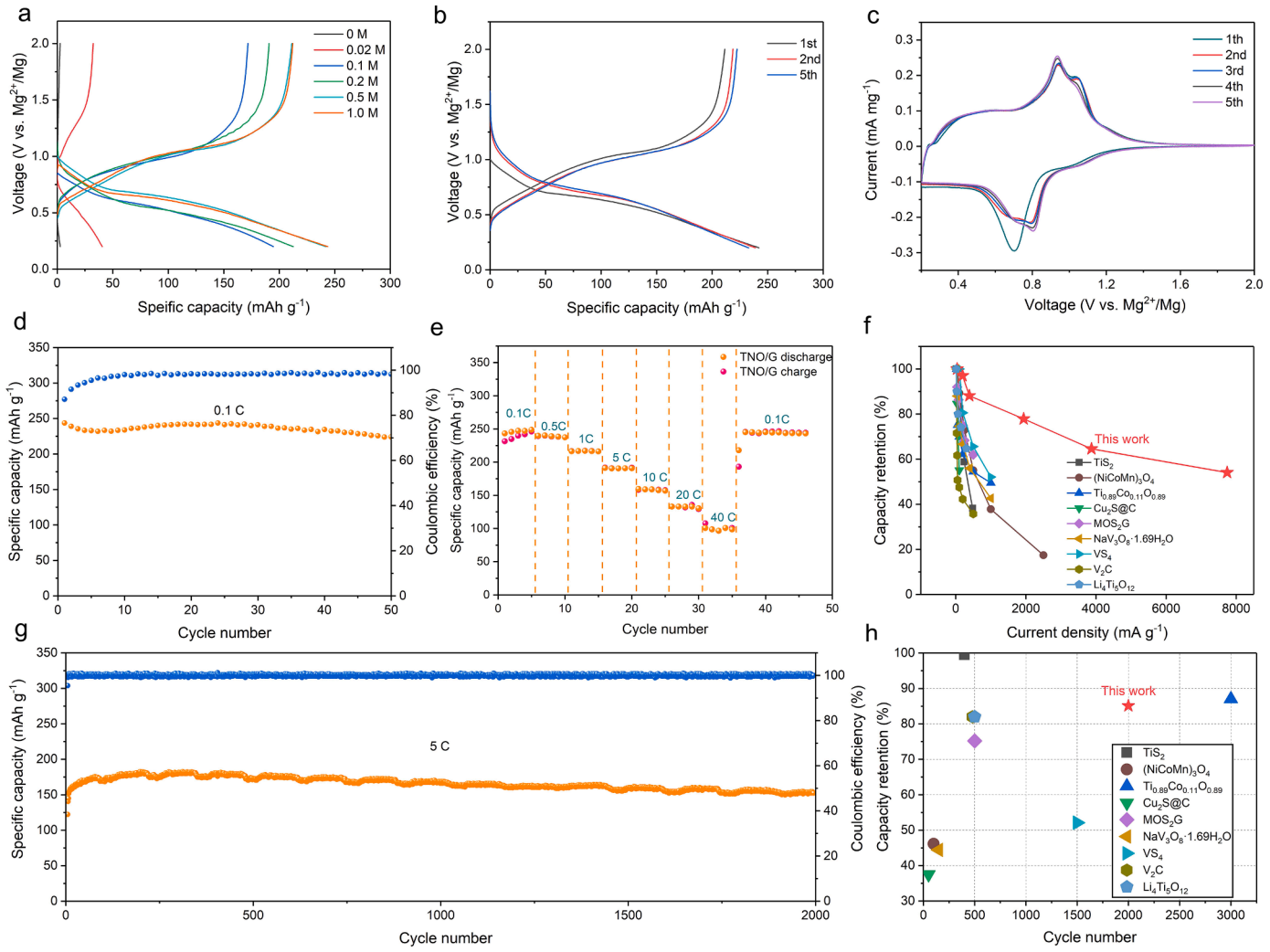

Fig. 3. (a) Voltage profiles of TNO/G in APC with different amounts of LiCl at 0.1 C. (b) Voltage profiles of the TNO/G in APC with 0.5 M LiCl at 0.1 C. (c) CV profiles of the TNO/G in APC with 0.5 M LiCl at 0.1 mV s^{-1}. (d) Cycling performance of the TNO/G in APC with 0.5 M LiCl at 0.1 C. (e) Rate performance of TNO/G in APC with 0.5 M LiCl. (f) Comparison between TNO/G and other advanced materials in hybrid Mg-Li batteries in terms of capacity retention at various current densities. (g) Long-cycle electrochemical performance of the TNO/G cathode in APC with 0.5 M LiCl at 5 C. (h) Comparison between TNO/G and other advanced materials in hybrid Mg-Li batteries in terms of long-term cycling stability.

diffusion kinetics of Mg^{2+}. The discharge capacity of TNO/G is significantly improved with the increase concentration of LiCl in APC. With only 0.02 M LiCl in APC, a discharge capacity of 40.5 mAh g^{-1} can be obtained. When the addition amount of LiCl is 0.1 M, the discharge capacity of TNO/G jumps to 194.6 mAh g^{-1}. The discharge capacity of TNO/G increases to 212.5 mAh g^{-1}, 242.0 mAh g^{-1} and 243.6 mAh g^{-1} with 0.2 M, 0.5 M and 1.0 M LiCl in APC, respectively. TNO/G exhibits remarkable electrochemical activity when the concentration of LiCl is 0.5 M and 1.0 M. Besides, TNO/G presents a lower polarization with addition of 0.5 M LiCl so 0.5 M LiCl in APC is chosen as the optimal electrolyte. And the charge-discharge curves of TNO/G in APC with 0.5 M LiCl at 0.1 C are shown in Fig. 3b. The pristine discharge and charge capacities of the TNO/G are 242.0 mAh g^{-1} and 211.4 mAh g^{-1}, corresponding to the coulombic efficiency of 87.3%. After 5 cycles, TNO/G exhibits a stable voltage curves and discharge capacity of 232.9 mAh g^{-1}, indicating the good reversibility of electrode material during cycling. As shown in Fig. 3c, cyclic voltammetry (CV) curves of the TNO/G in APC with 0.5 M LiCl show the distinct reaction potential. During the first cycle, the TNO/G presents a broad peak at 0.7 V vs. Mg^{2+}/Mg. However, starting from the second cycle, TNO/G shows two reduction peaks at 0.8 V and 0.7 V vs. Mg^{2+}/Mg, inferring that in addition to the intercalation of Li^+, Mg^{2+} may be inserted into the TNO/G with the assistance of LiCl. Therefore, CV profiles of the TNO/G at 0.1 mV s^{-1} in LIBs were also taken to verify this conjecture. As shown in **Fig. S6**, the TNO/G exhibits a set of redox peaks in LIBs with 301 electrolyte, which is in accordance with the reported results [37,39,48]. These results indicate that there may be the intercalation of Mg^{2+} in the TNO/G, which is achieved by the addition of LiCl in APC electrolyte. In order to confirm the existence of Mg^{2+}, the Inductively Coupled Plasma Atomic Emission Spectrometry (ICP-AES) results of discharged state TNO/G were collected. As shown in Table S1, when the TNO/G is discharged to 0.8 V at 0.1 C, the obvious Li and trace amounts of Mg can be detected and the molar ratio of Mg and Li is 0.0899, indicating that Li^+ is mainly intercalated into the TNO/G in former discharge process. After discharging to 0.7 V at 0.1 C, the contents of Li and Mg increase and the molar ratio of Mg and Li is 0.3178, indicating that Mg^{2+} and Li^+ are co-inserted into the TNO/G in this discharge process. Until the TNO/G is discharged to 0.2 V at 0.1 C, the insertion amount of Mg^{2+} and Li^+ reaches the maximum and the molar ratio of Mg and Li is 0.4498. When the TNO/G electrode is discharged to 0.2 V after 2, 5, and 10 cycles at 0.1 C, the molar ratio of n_{Mg}/n_{Li} are 0.4443, 0.4431, and 0.4206, respectively. The molar ratio of n_{Mg}/n_{Li} tends to stabilize after serval cycles. Besides, when the TNO/G electrode is discharged to 0.2 V after 10 cycles at 1 C and 5 C, the molar ratios of n_{Mg}/n_{Li} are 0.3324 and

0.2440, respectively, indicating that even at high rates, Mg^{2+} can still intercalate into TNO despite the decreased intercalation of Mg^{2+}.

As shown in Fig. 3d, TNO/G delivers a specific capacity of 224.1 mAh g^{-1} after 50 cycles (capacity retention of 92.0%). And TNO/G also presents the remarkable rate performance due to its unique structure. As shown in Fig. 3e, TNO/G exhibits discharge capacities of 246.0 mAh g^{-1}, 238.6 mAh g^{-1}, 216.8 mAh g^{-1}, 191.5 mAh g^{-1}, 158.9 mAh g^{-1} and 133.0 mAh g^{-1} at the density of 0.1 C, 0.5 C, 1 C, 5 C, 10 C, and 20 C, respectively. TNO/G even delivers the discharge capacity of 100.8 mAh g^{-1} at the current density of 40 C. It is worth noting that after the high-rate cycling at 40 C, TNO/G can still contribute discharge capacity of 245.7 mAh g^{-1} when the current density returns to 0.1 C. And the TNO/G exhibits better capacity retention at various current densities than other advanced materials in hybrid Mg-Li batteries, implying the outstanding rate performance of TNO/G in this battery system (Fig. 3f).

Besides, the TNO/G exhibits good cycling performance in APC with 0.5 M LiCl at 0.1 C. As shown in Fig. 3g, the long cycling performance of TNO/G at 5 C was tested. At the current density of 5 C, TNO/G can still deliver 152.4 mAh g^{-1} after 2000 cycles, corresponding to the capacity retention of 85.1%. When the current density raises to 10 C, TNO/G shows the remarkable cycling stability for 800 cycles and the discharge capacity of TNO/G remains at 142.9 mAh g^{-1} and no capacity decay is observed (**Fig. S7**). Obviously, Fig. 3h indicates that the long-term cycling stability of TNO/G cathode material in this battery system is comparable to other previously reported advanced materials in Mg-Li hybrid battery [49–57].

To explore the energy storage mechanism of TNO/G in APC with 0.5 M LiCl, ex-situ XRD measurements were conducted to verify the structure changes of the TNO/G. As shown in Fig. 4a–d, XRD patterns of TNO/G at different states are recorded. There are no peaks disappearing

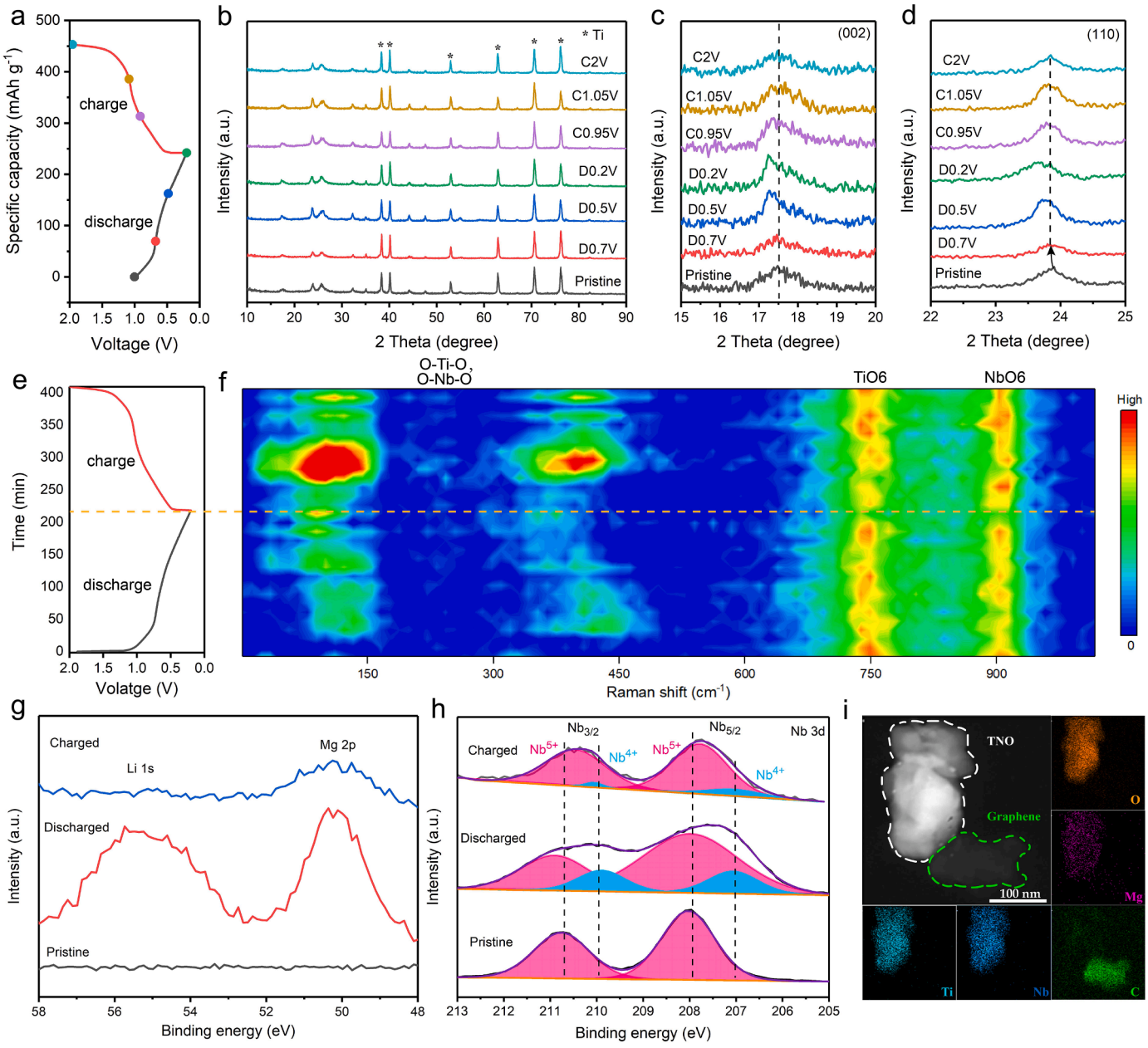

Fig. 4. (a) Voltage profiles of TNO/G at 0.1 C corresponding to ex-situ XRD tests. (b) XRD patterns of TNO/G at different states. (c, d) Local enlarged images of XRD patterns at different states. (e) The first-cycle voltage profiles of TNO/G corresponding to in-situ Raman measurements. (f) The simultaneous *in situ* electrochemical Raman spectra corresponding to (e). (g) Li 1s, Mg 2p, and (h) Nb 3d XPS spectra of the TNO/G electrode at different states. (i) Elemental mapping of TNO/G cathode material.

or new peaks appearing during the electrochemical tests, implying the electrochemical reaction mechanism of ions insertion/extraction in TNO/G. This result is consistent with the result of the previous article in LIBs [48]. When TNO/G is discharged to 0.2 V vs. Mg^{2+}/Mg, diffraction peak of the 002 plane shifts to a lower angle 17.27° from initial angle 17.49°, and diffraction peak of 110 plane shifts to a lower angle 23.68° from initial angle 23.90°, implying the intercalation of Li^{+}/Mg^{2+}. When TNO/G is charged to 2.0 V vs. Mg^{2+}/Mg, diffraction peak of the 002 plane shifts to the initial angle. Nevertheless, diffraction peak of the 110 plane returns to 23.84°, corresponding to the XRD pattern of the TNO/G electrode which is discharged to 0.7 V, implying that the intercalated ions are not completely released.

Moreover, in-situ Raman measurements were conducted to further confirm the reaction mechanism of TNO/G. As shown in Fig. 4e, f, the bands observed in the region < 500 cm^{-1} can be indexed to Nb-O and Ti-O vibrations and the bands observed around 750 cm^{-1} and 900 cm^{-1} belong to vibrations of the TiO_6 octahedra and the vibrations of the NbO_6 octahedra [58]. During the whole initial discharge/charge process, TiO_6 octahedra and NbO_6 octahedra exhibit equivalent intensity all the way, indicating the excellent overall structural stability of TNO/G. And the Nb-O and Ti-O bands present asymmetrical Raman spectra. When TNO/G is discharged to 0.7 V vs. Mg^{2+}/Mg, the Raman peaks of Nb-O and Ti-O bands shift to high angles, indicating the change of the local metal-O coordination structure of the TNO/G due to the ion intercalation. And when TNO/G is charged to 2 V vs. Mg^{2+}/Mg, the Raman spectrum of TNO/G is not consistent with the initial Raman spectrum of TNO/G. The asymmetric in-situ Raman spectra of TNO/G may be related to the incomplete extraction of ions, which is consistent with the results of ex-situ XRD measurements.

Furthermore, in order to further confirm the type of intercalated ions, the XPS spectra of the TNO/G at different states were collected. As shown in Fig. 4g, when the TNO/G is discharged to 0.2 V vs. Mg^{2+}/Mg, the characteristic peaks of Li 1s and Mg 2p appear, indicating the Li^{+}/Mg^{2+} co-insertion in TNO/G during the discharge process. When the TNO/G is charged to 2 V vs. Mg^{2+}/Mg, the characteristic peaks of Li 1s and Mg 2p are weakened, representing the extraction of Li^{+} and Mg^{2+} in the TNO/G. Furthermore, the XPS spectrum of charged state of TNO/G electrode proves that little Mg^{2+} are trapped inside the lattice of TNO/G, which may be caused by the electrostatic interaction between Mg^{2+} and lattice oxygen. Besides, with the insertion/extraction of ions, the valence state of Nb also changes. As shown in Fig. 4h, the characteristic peaks of Nb^{4+} (peaks at 209.8 eV and 207.0 eV) appear in the discharged state TNO/G, indicating the intercalation of ions. And when the TNO/G is charged to 2.0 V vs. Mg^{2+}/Mg, the valence state of most Nb returns to the Nb^{5+}, indicating the incomplete extraction of ions. These results are consistent with the results of in-situ Raman characterizations and ex-situ XRD tests. To further investigate the effect of irreversible structural changes on Mg^{2+} intercalation in TNO/G, the electrochemical behavior of fully charged TNO/G (MgTNO/G) after cycling in APC with 0.5 M LiCl was investigated. The battery of fully charged TNO/G after cycling in APC with 0.5 M LiCl was disassembled and MgTNO/G electrode was reassembled with pure APC electrolyte to observe the effects of irreversible structural changes. As shown in **Fig. S8**, the MgTNO/G exhibits lower polarization and slightly higher discharge capacity than TNO/G, indicating the irreversible structural changes do have an effect on improving Mg^{2+} intercalation. However, both of them exhibit the discharge capacity of no more than 20 mAh g^{-1}, implying that the irreversible structural changes are not the primary responsibility for improving electrochemical performance. Th results indicate that the Li^{+} pre-intercalation is still the dominant factor to improve the Mg storage capability of TNO/G. To further prove insertion of Mg^{2+}, energy dispersive spectroscopy (EDS) elemental mapping of the TNO/G at discharged state was obtained. As shown in Fig. 4i, elemental mapping results demonstrate that the Mg^{2+} has been successfully and uniformly inserted into the discharged TNO/G, implying the superiority of the Li^{+} pre-intercalation activation approach.

In order to get more insights into the unusual kinetic process in the charge storage mechanism of TNO/G, CV tests at 0.1 mV s^{-1}, 0.2 mV s^{-1}, 0.5 mV s^{-1}, 1 mV $s^{-1}$and 2 mV s^{-1} were performed. As shown in Fig. 5a, all the CV curves of TNO/G at variable scanning rates present the distinct redox peaks. Generally, the following Eqs. (3) and (4) are used to describe the relationship between peak current (i) and scan rate (v):

$$i = av^{b} \tag{3}$$

$$\log i = a + b\log v \tag{4}$$

Herein, a and b are adjustable parameters. When b tends to 0.5, the electrochemical process is controlled by semi-infinite diffusion. when b tends to 1, the electrochemical process is controlled by surface-controlled behavior. The calculated value of b is 0.816 by linear fitting, indicating that electrochemical process tends to be dominated by surface-controlled behavior (Fig. 5b). The percentages of capacitive contribution can be calculated according to Eq. (5) as follows:

$$i = k_1 v + k_2 v^{1/2} \tag{5}$$

in which $k_1 v$ and $k_2 v^{1/2}$ are ascribed to the capacitive contribution and diffusion-controlled contribution, respectively. Contribution ratios of the capacitive contribution and diffusion-controlled process at various scan rates are shown in Fig. 5c. When the scan rate goes from 0.1 to 2 mV s^{-1}, the percentage of capacitive contribution increases from 63.5 to 90.5%, indicating the electrochemical performance at high rate is mainly attributed to capacitive contribution.

Besides, in order to verify the high safety of the Mg anode at high current density, the SEM images of Mg foil were also taken to observe the morphological changes of the Mg anode side during the process of dissolution and deposition of Mg. As shown in Fig. 5d, the surface of fresh Mg anode is flat before cycling. After 800 cycles at 10 C, as shown in Fig. 5e, the surface of Mg anode is porous and uneven but not appearance of any dendrites, which implies that this battery system can work safely under high current density. To further describe the electrochemical behavior in TNO/G||APC+LiCl||Mg dual-ion battery, visible schematic illustration of the TNO/G||APC+LiCl||Mg dual-ion battery is shown in Fig. 5f. In this system, TNO/G serves as the cathode material, and Mg foil serves as the anode and reference electrode. APC with 0.5 M LiCl is used to the electrolyte. During the discharge process, Li^{+} is inserted in TNO/G firstly. Subsequently Li^{+} and Mg^{2+} are co-inserted inside the TNO/G. At the same time, Mg is dissolved on the side of anode. During the charge process, the reaction process is reversed. In conclusion, this battery system not only utilizes the rapid insertion and extraction of Li^{+} and Mg^{2+} on the cathode side, but also uses high-stability Mg foil as the anode, which greatly improves the long-term cycling performance and safety performance of the battery. These results demonstrate the superiority of Li^{+} per-intercalation activation approach.

4. Conclusions

In conclusion, the Li^{+} intercalation activated approach for realizing the highly reversible and rapid electrochemical kinetics of Mg^{2+} in Ti-Nb oxides is proposed in this work. The preceding intercalation of Li^{+} can not only enhance the electronic conductivity of TNO, but also reduce the diffusion energy barrier of Mg^{2+} simultaneously, benefitting to subsequent intercalation of ions. Meanwhile. the pre-intercalated Li^{+} can also alleviate the volume change caused by the intercalation of Mg^{2+} into TNO, achieving the excellent structural stability during ions (de) intercalation processes. Consequently, the synchronous manipulation of electron transport, ion diffusion and structural integrity of TNO leads to an outstanding electrochemical performance. This work is expected to open up the new insights for fast charge/discharge and high-safety Mg-Li dual-ion batteries and shed light on the potential application of the Mg-Li dual-ion batteries in large-scale energy storages.

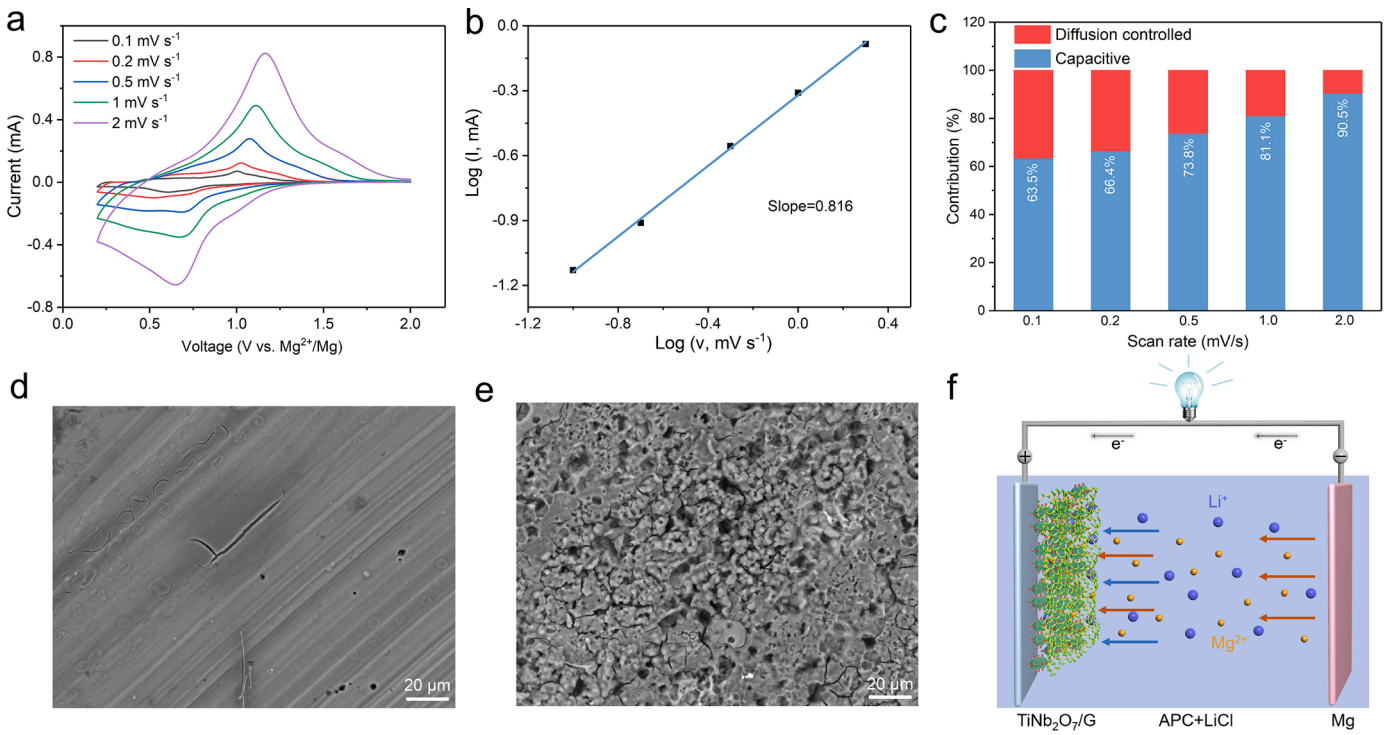

Fig. 5. (a) CV profiles of TNO/G. (b) The fitted lines of the peak current and scan rate. (c) Contribution ratio of the capacitive contribution and diffusion-controlled process. (d) SEM image of fresh Mg foil. (e) SEM image of Mg anode after 800 cycles at 10 C. (f) Schematic illustration of the TNO/G||APC+LiCl||Mg dual-ion battery.

Supplementary materials

Discharge and charge profiles; Theoretical calculations; XPS spectra; CV curves; Cycling performance; ICP results.

CRediT authorship contribution statement

Dongzheng Wu: Conceptualization, Methodology, Investigation, Software, Writing – original draft. **Fei Wang:** Investigation, Formal analysis. **Huiya Yang:** Methodology. **Yaoqi Xu:** Validation. **Yichao Zhuang:** Validation. **Jing Zeng:** Supervision, Writing – review & editing, Funding acquisition. **Yang Yang:** Supervision, Writing – review & editing, Project administration, Funding acquisition. **Jinbao Zhao:** Supervision, Writing – review & editing, Funding acquisition.

Declaration of Competing Interest

The authors declare that they have no known competing financial interests or personal relationships that could have appeared to influence the work reported in this paper.

Data Availability

Data will be made available on request.

Acknowledgments

The authors gratefully acknowledge the National Natural Science Foundation of China (21875198, 22005257, 22109030, and 22021001), Natural Science Foundation of Fujian Province of China (2020J05009), Guangdong Basic and Applied Basic Research Foundation (2021A1515010177) and the Key Research and Development Program of Yunnan Province (202103AA080019) for financial support. The authors also would like to thank Ms. Y. H. Kang for support of partial theoretical calculation.

Supplementary materials

Supplementary material associated with this article can be found, in the online version, at doi:10.1016/j.ensm.2022.07.042.

References

[1] J. Teng, Q. Wang, L. Zhang, H. Zhang, X. Chen, P. Zhang, J. Zhao, Influence of heat treatment time on cathode material Cr_8O_{21} for lithium battery, J. Electrochem. 27 (2021) 689–697, https://doi.org/10.13208/j.electrochem.210121.
[2] J.B. Goodenough, K.-S. Park, The Li-ion rechargeable battery: a perspective, J. Am. Chem. Soc. 135 (2013) 1167–1176, https://doi.org/10.1021/ja3091438.
[3] J. Hao, J. Zhang, G. Xia, Y. Liu, Y. Zheng, W. Zhang, Y. Tang, W.K. Pang, Z. Guo, Heterostructure manipulation via *in situ* localized phase transformation for high-rate and highly durable lithium ion storage, ACS Nano 12 (2018) 10430–10438, https://doi.org/10.1021/acsnano.8b06020.
[4] S. Zhang, Y. Zheng, X. Huang, J. Hong, B. Cao, J. Hao, Q. Fan, T. Zhou, Z. Guo, Structural engineering of hierarchical micro-nanostructured Ge–C framework by controlling the nucleation for ultralong-life Li storage, Adv. Energy Mater. 9 (2019), 1900081, https://doi.org/10.1002/aenm.201900081.
[5] F. Wu, N. Chen, R. Chen, Q. Zhu, G. Tan, L. Li, Self-regulative nanogelator solid electrolyte: a new option to improve the safety of lithium battery, Adv. Sci. 3 (2016), 1500306, https://doi.org/10.1002/advs.201500306.
[6] G.-L. Xu, Q. Liu, K.K.S. Lau, Y. Liu, X. Liu, H. Gao, X. Zhou, M. Zhuang, Y. Ren, J. Li, M. Shao, M. Ouyang, F. Pan, Z. Chen, K. Amine, G. Chen, Building ultraconformal protective layers on both secondary and primary particles of layered lithium transition metal oxide cathodes, Nat. Energy 4 (2019) 484–494, https://doi.org/10.1038/s41560-019-0387-1.
[7] X. Feng, M. Ouyang, X. Liu, L. Lu, Y. Xia, X. He, Thermal runaway mechanism of lithium ion battery for electric vehicles: a review, Energy Storage Mater. 10 (2018) 246–267, https://doi.org/10.1016/j.ensm.2017.05.013.
[8] Q. Wang, L. Jiang, Y. Yu, J. Sun, Progress of enhancing the safety of lithium ion battery from the electrolyte aspect, Nano Energy 55 (2019) 93–114, https://doi.org/10.1016/j.nanoen.2018.10.035.
[9] L. Cui, L. Zhou, K. Zhang, F. Xiong, S. Tan, M. Li, Q. An, Y.M. Kang, L. Mai, Salt-controlled dissolution in pigment cathode for high-capacity and long-life magnesium organic batteries, Nano Energy 65 (2019), 103902, https://doi.org/10.1016/j.nanoen.2019.103902.
[10] Y. Liang, R. Feng, S. Yang, H. Ma, J. Liang, J. Chen, Rechargeable Mg batteries with graphene-like MoS_2 cathode and ultrasmall Mg nanoparticle anode, Adv. Mater. 23 (2011) 640–643, https://doi.org/10.1002/adma.201003560.
[11] Y. Wang, Z. Liu, C. Wang, X. Yi, R. Chen, L. Ma, Y. Hu, G. Zhu, T. Chen, Z. Tie, J. Ma, J. Liu, Z. Jin, Highly branched VS_4 nanodendrites with 1D atomic-chain structure as a promising cathode material for long-cycling magnesium batteries, Adv. Mater. 30 (2018), 1802563, https://doi.org/10.1002/adma.201802563.

[12] Y. Wang, X. Xue, P. Liu, C. Wang, X. Yi, Y. Hu, L. Ma, G. Zhu, R. Chen, T. Chen, J. Ma, J. Liu, Z. Jin, Atomic substitution enabled synthesis of vacancy-rich two-dimensional black TiO_2_x nanoflakes for high-performance rechargeable magnesium batteries, ACS Nano 12 (2018) 12492–12502, https://doi.org/10.1021/acsnano.8b06917.

[13] R. Singh, S. Janakiraman, A. Agrawal, S. Ghosh, A. Venimadhav, K. Biswas, An amorphous poly(vinylidene fluoride-co-hexafluoropropylene) based gel polymer electrolyte for magnesium ion battery, J. Electroanal. Chem. 858 (2020), 113788, https://doi.org/10.1016/j.jelechem.2019.113788.

[14] Y. Shen, Y. Wang, Y. Miao, M. Yang, X. Zhao, X. Shen, High-energy interlayer-expanded copper sulfide cathode material in non-corrosive electrolyte for rechargeable magnesium batteries, Adv. Mater. 32 (2020), 1905524, https://doi.org/10.1002/adma.201905524.

[15] Y. Li, X. Zhou, J. Hu, Y. Zheng, M. Huang, K. Guo, C. Li, Reversible Mg metal anode in conventional electrolyte enabled by durable heterogeneous SEI with low surface diffusion barrier, Energy Storage Mater. 46 (2022) 1–9, https://doi.org/10.1016/j.ensm.2021.12.023.

[16] Y. Xu, Z. Liu, X. Zheng, K. Li, M. Wang, W. Yu, H. Hu, W. Chen, Solid electrolyte interface regulated by solvent-in-water electrolyte enables high-voltage and stable aqueous Mg-MnO_2 batteries, Adv. Energy Mater. (2022), 2103352, https://doi.org/10.1002/aenm.202103352.

[17] H. Li, T. Ichitsubo, S. Yagi, E. Matsubara, Constructing metal-anode rechargeable batteries utilizing concomitant intercalation of Li–Mg dual cations into Mo_6S_8, J. Mater. Chem. A 5 (2017) 3534–3540, https://doi.org/10.1039/C6TA10663C.

[18] H. Li, N.L. Okamoto, T. Hatakeyama, Y. Kumagai, F. Oba, T. Ichitsubo, Fast diffusion of multivalent ions facilitated by concerted interactions in dual-ion battery systems, Adv. Energy Mater. 8 (2018), 1801475, https://doi.org/10.1002/aenm.201801475.

[19] D. Aurbach, G.S. Suresh, E. Levi, A. Mitelman, O. Mizrahi, O. Chusid, M. Brunelli, Progress in rechargeable magnesium battery technology, Adv. Mater. 19 (2007) 4260–4267, https://doi.org/10.1002/adma.200701495.

[20] C. Du, W. Younas, Z. Wang, X. Yang, E. Meng, L. Wang, J. Huang, X. Ma, Y. Zhu, C. Cao, Constructing sheet-assembled hollow CuSe nanocubes to boost the rate capability of rechargeable magnesium batteries, J. Mater. Chem. A 9 (2021) 3648–3656, https://doi.org/10.1039/D0TA10708E.

[21] C. Zuo, W. Tang, B. Lan, F. Xiong, H. Tang, S. Dong, W. Zhang, C. Tang, J. Li, Y. Ruan, S. Xi, Q. An, P. Luo, Unexpected discovery of magnesium-vanadium spinel oxide containing extractable Mg^{2+} as a high-capacity cathode material for magnesium ion batteries, Chem. Eng. J. 405 (2021), 127005, https://doi.org/10.1016/j.cej.2020.127005.

[22] A. Du, H. Zhang, Z. Zhang, J. Zhao, Z. Cui, Y. Zhao, S. Dong, L. Wang, X. Zhou, G. Cui, A crosslinked polytetrahydrofuran-borate-based polymer electrolyte enabling wide-working-temperature-range rechargeable magnesium batteries, Adv. Mater. 31 (2019), 1805930, https://doi.org/10.1002/adma.201805930.

[23] X. Cheng, Z. Zhang, Q. Kong, Q. Zhang, T. Wang, S. Dong, L. Gu, X. Wang, J. Ma, P. Han, H. Lin, C. Chen, G. Cui, Highly reversible cuprous mediated cathode chemistry for magnesium batteries, Angew. Chem. Int. Ed. 59 (2020) 11477–11482, https://doi.org/10.1002/anie.202002177.

[24] X. Xue, R. Chen, C. Yan, P. Zhao, Y. Hu, W. Kong, H. Lin, L. Wang, Z. Jin, One-step synthesis of 2-ethylhexylamine pillared vanadium disulfide nanoflowers with ultralarge interlayer spacing for high-performance magnesium storage, Adv. Energy Mater. 9 (2019), 1900145, https://doi.org/10.1002/aenm.201900145.

[25] Y. Wang, Z. Liu, C. Wang, Y. Hu, H. Lin, W. Kong, J. Ma, Z. Jin, π-Conjugated polyimide-based organic cathodes with extremely-long cycling life for rechargeable magnesium batteries, Energy Storage Mater. 26 (2020) 494–502, https://doi.org/10.1016/j.ensm.2019.11.023.

[26] Y. Xu, X. Deng, Q. Li, G. Zhang, F. Xiong, S. Tan, Q. Wei, J. Lu, J. Li, Q. An, L. Mai, Vanadium oxide pillared by interlayer Mg^{2+} ions and water as ultralong-life cathodes for magnesium-ion batteries, Chemistry 5 (2019) 1194–1209, https://doi.org/10.1016/j.chempr.2019.02.014.

[27] H. Dong, O. Tutusaus, Y. Liang, Y. Zhang, Z. Lebens-Higgins, W. Yang, R. Mohtadi, Y. Yao, High-power Mg batteries enabled by heterogeneous enolization redox chemistry and weakly coordinating electrolytes, Nat. Energy 5 (2020) 1043–1050, https://doi.org/10.1038/s41560-020-00734-0.

[28] N. Wu, Y.X. Yin, Y.G. Guo, Size-dependent electrochemical magnesium storage performance of spinel lithium titanate, Chem. Asian J. 9 (2014) 2099–2102, https://doi.org/10.1002/asia.201402286.

[29] Y. Liang, H.D. Yoo, Y. Li, J. Shuai, H.A. Calderon, F.C. Robles Hernandez, L. C. Grabow, Y. Yao, Interlayer-expanded molybdenum disulfide nanocomposites for electrochemical magnesium storage, Nano Lett. 15 (2015) 2194–2202, https://doi.org/10.1021/acs.nanolett.5b00388.

[30] M. Xu, S. Lei, J. Qi, Q. Dou, L. Liu, Y. Lu, Q. Huang, S. Shi, X. Yan, Opening magnesium storage capability of two-dimensional MXene by intercalation of cationic surfactant, ACS Nano 12 (2018) 3733–3740, https://doi.org/10.1021/acsnano.8b00959.

[31] L. Zhou, Q. Liu, Z. Zhang, K. Zhang, F. Xiong, S. Tan, Q. An, Y.M. Kang, Z. Zhou, L. Mai, Interlayer-spacing-regulated $VOPO_4$ nanosheets with fast kinetics for high-capacity and durable rechargeable magnesium batteries, Adv. Mater. 30 (2018), 1801984, https://doi.org/10.1002/adma.201801984.

[32] H. Tang, F. Xiong, Y. Jiang, C. Pei, S. Tan, W. Yang, M. Li, Q. An, L. Mai, Alkali ions pre-intercalated layered vanadium oxide nanowires for stable magnesium ions storage, Nano Energy 58 (2019) 347–354, https://doi.org/10.1016/j.nanoen.2019.01.053.

[33] Z. Wang, Y. Zhu, H. Peng, C. Du, X. Ma, C. Cao, Microwave-induced phase engineering of copper sulfide nanosheets for rechargeable magnesium batteries, Electrochim. Acta 374 (2021), 137965, https://doi.org/10.1016/j.electacta.2021.137965.

[34] M. Mao, X. Ji, S. Hou, T. Gao, F. Wang, L. Chen, X. Fan, J. Chen, J. Ma, C. Wang, Tuning anionic chemistry to improve kinetics of Mg intercalation, Chem. Mater. 31 (2019) 3183–3191, https://doi.org/10.1021/acs.chemmater.8b05218.

[35] Y. Ma, Y. Zhang, F. Wang, H. Xie, J. Wang, Bimetallic sulfide $NiCo_2S_4$ yolk–shell nanospheres as high-performance cathode materials for rechargeable magnesium batteries, Nanoscale 14 (2022) 4753–4761, https://doi.org/10.1039/D2NR00128D.

[36] J.-T. Han, Y.-H. Huang, J.B. Goodenough, New anode framework for rechargeable lithium batteries, Chem. Mater. 23 (2011) 2027–2029, https://doi.org/10.1021/cm200441h.

[37] Y. Yang, J. Huang, Z. Cao, Z. Lv, D. Wu, Z. Wen, W. Meng, J. Zeng, C.C. Li, J. Zhao, Synchronous manipulation of ion and electron transfer in wadsley–roth Phase Ti-Nb oxides for fast-charging lithium-ion batteries, Adv. Sci. 9 (2022), 2104530, https://doi.org/10.1002/advs.202104530.

[38] Z. Lv, H. Zhu, W. Meng, L. Wei, Y. Yang, Y. Zhang, M. Ye, C.C. Li, Cation mixing in Wadsley-Roth phase anode of lithium-ion battery improves cycling stability and fast Li^+ storage, Appl. Phys. Rev. 8 (2021), 031404, https://doi.org/10.1063/5.0054030.

[39] S. Lou, X. Cheng, Y. Zhao, A. Lushington, J. Gao, Q. Li, P. Zuo, B. Wang, Y. Gao, Y. Ma, C. Du, G. Yin, X. Sun, Superior performance of ordered macroporous $TiNb_2O_7$ anodes for lithium ion batteries: understanding from the structural and pseudocapacitive insights on achieving high rate capability, Nano Energy 34 (2017) 15–25, https://doi.org/10.1016/j.nanoen.2017.01.058.

[40] K. Tang, X. Mu, P.A. van Aken, Y. Yu, J. Maier, Nano-pearl-string" $TiNb_2O_7$ as anodes for rechargeable lithium batteries, Adv. Energy Mater. 3 (2013) 49–53, https://doi.org/10.1002/aenm.201200396.

[41] X. Miao, J. Yang, W. Pan, H. Yuan, Y. Nuli, S. Hirano, Graphite fluoride as a cathode material for primary magnesium batteries with high energy density, Electrochim. Acta 210 (2016) 704–711, https://doi.org/10.1016/j.electacta.2016.05.198.

[42] G. Kresse, J. Hafner, Ab initio molecular-dynamics simulation of the liquid-metal–amorphous-semiconductor transition in germanium, Phys. Rev. B 49 (1994) 14251–14269, https://doi.org/10.1103/PhysRevB.49.14251.

[43] P.E. Blöchl, Projector augmented-wave method, Phys. Rev. B 50 (1994) 17953–17979, https://doi.org/10.1103/PhysRevB.50.17953.

[44] B. Hammer, L.B. Hansen, J.K. Nørskov, Improved adsorption energetics within density-functional theory using revised Perdew-Burke-Ernzerhof functionals, Phys. Rev. B 59 (1999) 7413–7421, https://doi.org/10.1103/PhysRevB.59.7413.

[45] G. Henkelman, H. Jónsson, Improved tangent estimate in the nudged elastic band method for finding minimum energy paths and saddle points, J. Chem. Phys. 113 (2000) 9978–9985, https://doi.org/10.1063/1.1323224.

[46] D. Sheppard, R. Terrell, G. Henkelman, Optimization methods for finding minimum energy paths, J. Chem. Phys. 128 (2008), 134106, https://doi.org/10.1063/1.2841941.

[47] C.P. Koçer, K.J. Griffith, C.P. Grey, A.J. Morris, Lithium diffusion in niobium tungsten oxide shear structures, Chem. Mater. 32 (2020) 3980–3989, https://doi.org/10.1021/acs.chemmater.0c00483.

[48] H. Yu, H. Lan, L. Yan, S. Qian, X. Cheng, H. Zhu, N. Long, M. Shui, J. Shu, $TiNb_2O_7$ hollow nanofiber anode with superior electrochemical performance in rechargeable lithium ion batteries, Nano Energy 38 (2017) 109–117, https://doi.org/10.1016/j.nanoen.2017.05.057.

[49] T. Gao, F. Han, Y. Zhu, L. Suo, C. Luo, K. Xu, C. Wang, Hybrid Mg^{2+}/Li^+ battery with long cycle life and high rate capability, Adv. Energy Mater. 5 (2015), 1401507, https://doi.org/10.1002/aenm.201401507.

[50] M. Asif, M. Rashad, Z. Ali, I. Ahmed, Synthesis of ternary metal oxides as positive electrodes for Mg–Li hybrid ion batteries, Nanoscale 12 (2020) 924–932, https://doi.org/10.1039/C9NR08758C.

[51] M. Vincent, V.S. Avvaru, M. Haranczyk, V. Etacheri, High-performance Mg−Li hybrid batteries based on pseudocapacitive anatase Ti_1_x$CoxO_2$_y nanosheet cathodes, ChemSusChem (2022) 15, https://doi.org/10.1002/cssc.202102562.

[52] W. Wang, Y. Yang, Y. NuLi, J. Zhou, J. Yang, J. Wang, Metal organic framework (MOF)-derived carbon-encapsulated cuprous sulfide cathode based on displacement reaction for Hybrid Mg^{2+}/Li^+ batteries, J. Power Sources 445 (2020), 227325, https://doi.org/10.1016/j.jpowsour.2019.227325.

[53] X. Fan, R.R. Gaddam, N.A. Kumar, X.S. Zhao, A hybrid Mg^{2+}/Li^+ battery based on interlayer-expanded MoS_2/graphene cathode, Adv. Energy Mater. 7 (2017), 1700317, https://doi.org/10.1002/aenm.201700317.

[54] M. Rashad, X. Li, H. Zhang, Magnesium/lithium-ion hybrid battery with high reversibility by employing NaV_3O_8 1.69H_2O nanobelts as a positive electrode, ACS Appl. Mater. Interfaces 10 (2018) 21313–21320, https://doi.org/10.1021/acsami.8b04139.

[55] Y. Wang, C. Wang, X. Yi, Y. Hu, L. Wang, L. Ma, G. Zhu, T. Chen, Z. Jin, Hybrid Mg/Li-ion batteries enabled by Mg^{2+}/Li^+ co-intercalation in VS_4 nanodendrites, Energy Storage Mater. 23 (2019) 741–748, https://doi.org/10.1016/j.ensm.2019.06.001.

[56] F. Liu, Y. Liu, X. Zhao, K. Liu, H. Yin, L. Fan, Prelithiated V_2C MXene: a high-performance electrode for hybrid magnesium/lithium-ion batteries by ion

cointercalation, Small 16 (2020), 1906076, https://doi.org/10.1002/smll.201906076.
[57] N. Wu, Z.Z. Yang, H.R. Yao, Y.X. Yin, L. Gu, Y.G. Guo, Improving the electrochemical performance of the $Li_4Ti_5O_{12}$ electrode in a rechargeable magnesium battery by lithium-magnesium co-intercalation, Angew. Chem. Int. Ed. 54 (2015) 5757–5761, https://doi.org/10.1002/anie.201501005.
[58] N.G. Eror, U. Balachandran, Coordination of cations in $TiNb_2O_7$ by raman spectroscopy, J. Solid State Chem. 45 (1982) 276–279, https://doi.org/10.1016/0022-4596(82)90283-3.